

Defocus to focus: photo-realistic bokeh rendering by fusing defocus and radiance priors

Xianrui Luo^{a,1}, Juewen Peng^{a,1}, Ke Xian^a, Zijin Wu^a, Zhiguo Cao^{a,*}

^a*Key Laboratory of Image Processing and Intelligent Control, Ministry of Education;
School of Artificial Intelligence and Automation, Huazhong University of Science and
Technology, Wuhan, 430074, PR China*

Abstract

We consider the problem of realistic bokeh rendering from a single all-in-focus image. Bokeh rendering mimics aesthetic shallow depth-of-field (DoF) in professional photography, but these visual effects generated by existing methods suffer from simple flat background blur and blurred in-focus regions, giving rise to unrealistic rendered results. In this work, we argue that realistic bokeh rendering should i) model depth relations and distinguish in-focus regions, ii) sustain sharp in-focus regions, and iii) render physically accurate Circle of Confusion (CoC). To this end, we present a Defocus to Focus (D2F) framework to learn realistic bokeh rendering by fusing defocus priors with the all-in-focus image and by implementing radiance priors in layered fusion. Since no depth map is provided, we introduce defocus hallucination to integrate depth by learning to focus. The predicted defocus map implies the blur amount of bokeh and is used to guide weighted layered

*Corresponding author

Email addresses: xianruiluo@hust.edu.cn (Xianrui Luo),
juewenpeng@hust.edu.cn (Juewen Peng), kexian@hust.edu.cn (Ke Xian),
zijinwu@hust.edu.cn (Zijin Wu), zgcao@hust.edu.cn (Zhiguo Cao)

¹(Xianrui Luo and Juewen Peng contributed equally to this work.)

rendering. In layered rendering, we fuse images blurred by different kernels based on the defocus map. To increase the reality of the bokeh, we adopt radiance virtualization to simulate scene radiance. The scene radiance used in weighted layered rendering reassigns weights in the soft disk kernel to produce the CoC. To ensure the sharpness of in-focus regions, we propose to fuse upsampled bokeh images and original images. We predict the initial fusion mask from our defocus map and refine the mask with a deep network. We evaluate our model on a large-scale bokeh dataset. Extensive experiments show that our approach is capable of rendering visually pleasing bokeh effects in complex scenes. In particular, our solution receives the runner-up award in the AIM 2020 Rendering Realistic Bokeh Challenge.

Keywords: Bokeh rendering, Image fusion, Circle of confusion, Defocus estimation, Deep blending

1. Introduction

Bokeh, sometimes known as shallow depth of field (DoF), is an important aesthetic feature for photographers, which is popular in videography, portraiture, and landscape photography. Bokeh is closely related to focusing. In a camera shot, focusing refers to the process of adjusting the camera lens so that a scene at a certain distance from the camera is clearly imaged. By contrast, generating bokeh is conventionally recognized as blurring out-of-focus regions and producing delightful “bokeh balls”. The bokeh balls, which are also referred to as the Circle of Confusion (CoC), is one of the factors that affect the artistic quality of captured images. The CoC is shaped according to how a lens renders light from out-of-focus areas, and regularly, is viewed



Figure 1. **Comparison of different bokeh rendering approaches.** Mainstream bokeh rendering methods such as PyNET [1] cannot explicitly synthesize the Circle of Confusion (CoC) and sometimes can slightly blur in-focus regions. To synthesize the CoC, we present a novel Defocus to Focus (D2F) framework that modulates bokeh with estimated depth and predicted scene radiance. During exploration, we find that the blurred in-focus regions are mainly due to the naive treatment of upsampling. We show that this can be addressed in D2F with deep gradient-based image fusion.

as a disc based on the shape of the aperture. In photography, the aperture of a camera is used to control the amount of light that passes through the lens

and thus the exposure of the photosensitive sensor; a wide aperture allows more light to travel, which results in shallow DoF. However, not all shallow DoF is equivalent to bokeh. Shallow DoF often blurs the background, but only the blurred background with artistic patterns can be called bokeh.

Bokeh is mostly rendered from an expensive digital single-lens reflex (DSLR) camera by professional photographers, and the settings used to sharpen in-focus areas and to blur the rest require complicated maneuvers. The costs of operation time and expensive hardware hinder easy application of bokeh to amateurs. The desire to easily operate bokeh has therefore motivated enthusiasm for vision-based bokeh rendering.

Prior work has come up with several ideas to address bokeh rendering. One is to use stereo pairs to obtain disparity maps and to render bokeh; however, it requires extra dual-pixel sensors [3] or laser scanners [4]. Another alternative is deep learning-based neural rendering [1, 5], where methods are proposed to synthesize blur only from a single all-in-focus image. However, most existing models overlook two factors in photo-realistic bokeh rendering: 1) the rendering of CoC, an important artistic feature in bokeh, and 2) the sharpness of focused regions. Failing to render them can engender unrealistic effects, as shown in Fig. 1.

In this work, we are interested in single-image bokeh rendering. To render photo-realistic bokeh effects, we consider an effective single-image bokeh rendering approach should i) construct correct relative depth relation and perceive in-focus regions, ii) render the physically sound CoC, and iii) maintain the sharpness of focused regions. Indeed rendering requires accurate depth and focusing to imply an appropriate blur amount of each pixel. We

aim to integrate these two steps to simplify the pipeline. To address the rendering of CoC, we modify our layered rendering which fuses blurred images with different blur levels. The change is that we reassign weights in rendering, which follows the idea of scene radiance [6] and manually recovers high dynamic range (HDR) [7] to synthesize realistic shallow DoF where image intensity is transformed into radiance in HDR. In addition, to render the CoC naturally, we design a new disk-like blur kernel. Finally, to keep the sharpness of in-focus regions during upsampling, we propose to execute image fusion beyond naive interpolation. We utilize the predicted defocus map and Poisson gradient constraint as guidance for the fusion mask.

To this end, we present Defocus to Focus (D2F), a fusion framework for photo-realistic bokeh rendering (Fig. 2). In particular, we introduce *defocus hallucination* to implement relative depth prediction and focusing. We use the term ‘hallucination’ instead of ‘estimation’ because the predicted defocus map is ‘imagined’ without direct supervision. The imagined defocus map is equivalent to the absolute value of a signed depth map that unifies relative depth and focal distance (‘ > 0 ’ indicates the region-to-camera distance is further than focal distance, ‘ < 0 ’ suggests the distance is closer than focal distance, and ‘ $= 0$ ’ implies the distance is equal to focal distance). The defocus map is then used as a guidance for *weighted layered rendering*. Compared to layered rendering which fuses images blurred by different blur kernels, we harness scene radiance within pixels and manually set them in HDR to synthesize the CoC. Hence, a *radiance virtualization* module is designed to predict scene radiance, and we choose soft disk blur kernels to increase the reality of CoC. For efficiency, defocus hallucination and radiance

virtualization are jointly learned to render bokeh in low resolution.

To recover the resolution of the rendered result, we propose a novel *deep Poisson fusion* designated for bokeh rendering. We predict the fusion mask by applying the defocus map and training a deep Poisson network. We maintain clear in-focus regions from blurred backgrounds and ensure smooth transitions between them.

Extensive experiments are conducted to validate D2F quantitatively and qualitatively. We evaluate D2F on the AIM 2020 Rendering Realistic Bokeh Challenge where a large-scale dataset called EBB! [1] is used. Results show that D2F achieves competitive results against well-established baselines and competition entries. Specifically, D2F increases PSNR by 0.17dB than our previous work [2]. To evaluate the performance of the fusion method, we compare our fusion module with other image fusion methods. Our fusion method is proved to outperform other methods. We also design ablation studies to prove the effectiveness of each module. Furthermore, we show the superiority of the soft disk blur kernel over the naive one in generating realistic CoC through qualitative visualizations, where the soft blur kernel appears more like a disk. In addition, we compare different training strategies to examine convergence behaviors. Our experiments support that D2F can render photo-realistic bokeh.

Our main contributions include the following:

- D2F: a novel framework which integrates defocus and radiance priors into photo-realistic bokeh rendering. We also apply Poisson fusion to keep the sharpness of in-focus objects;
- Defocus Hallucination: a scheme that learns relative depth and focal dis-

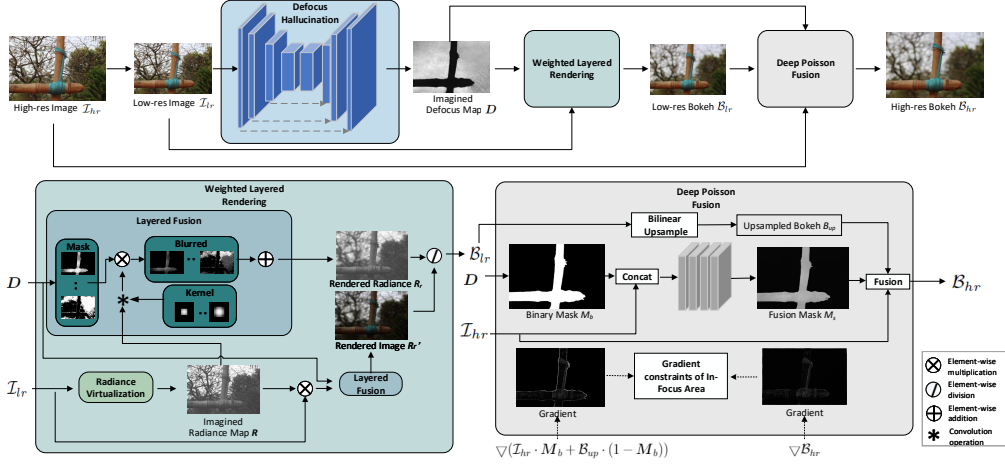


Figure 2. **Technical pipeline of D2F.** D2F renders photo-realistic bokeh by fusing defocus and radiance priors. In particular, a defocus map D and a radiance map \mathcal{R} are first predicted with defocus hallucination and radiance virtualization from the low resolution all-in-focus image \mathcal{I}_{lr} , respectively, where \mathcal{I}_{lr} is downsampled from its high-resolution counterpart \mathcal{I}_{hr} . Layered fusion then receives two groups of inputs: i) \mathcal{R} -weighted \mathcal{I}_{lr} and D , and ii) \mathcal{R} and D . Next the output \mathcal{R}_r and \mathcal{R}'_r are used to modulate the low-resolution bokeh \mathcal{B}_{lr} . We bilinearly upsample \mathcal{B}_{lr} to generate \mathcal{B}_{up} . Finally, we use deep Poisson fusion to generate a mask M_s for the fusion of the all-in-focus image \mathcal{I}_{hr} and \mathcal{B}_{up} . It is worth mentioning that our fusion method produces the mask with the help of D and a deep Poisson network. This fusion method maintains the sharpness of in-focus area of \mathcal{B}_{hr} during upsampling of \mathcal{B}_{lr} .

tance without direct supervision. The defocus map defines the degree of blurring of each pixel, so we can manually change the focal plane as well as the blur amount.

- We employ defocus hallucination in deep Poisson fusion, where we predict the fusion mask from the predicted defocus map and Poisson gradient constraint.

The preliminary version of this work appeared in [2], which describes our runner-up solution in the AIM 2020 Rendering Realistic Bokeh Challenge. Here we extend [2] in the following aspects. First, we simplify the training scheme for fast convergence. Second, we address the remaining issue of our

previous pipeline by employing image fusion with the help of a defocus map and a deep Poisson network. Our fusion module can keep the sharpness of in-focus objects. Third, we conduct additional experiments and analyses to justify the design choices and the soundness of our inclusions in the D2F framework.

2. Related Work

2.1. Defocus Estimation

Defocus estimation is closely related to depth estimation [8, 9] and defocus blur detection [10, 11]. While defocus detection focuses on whether the pixel is blurred, the defocus map from defocus estimation represents the amount of defocus blur in shallow DoF images, which has many applications such as image deblurring [12], blur magnification [13], and depth estimation [14, 15, 16, 17, 18]. Defocus estimation can be categorized into two types: region based and edge based.

Region based methods directly use image patches to estimate the defocus blur. In particular, some works [16, 19] focus on detecting small blur amount. Yan *et al.* [20] apply a neural network to predict the blur type and its parameters. Tang *et al.* [21] use log averaged spectrum residual to obtain a coarse defocus map and refine it iteratively by exploiting the relevance of similar neighbor regions.

In edge based paradigms, an early attempt [22] predicts the blur amount around edges from the ratio of gradients between original and blurred images, then interpolation from Laplacian matting [23] is applied to recover the defocus map. Xu *et al.* [24] also use Laplacian matting [23], but esti-

mate a sparse defocus map from metric ranks of local patches in the gradient domain. Kumar *et al.* [25] estimate motion blur and defocus blur jointly. Park *et al.* [26] introduce various hand-crafted features and deep features to produce defocus map from multi-scale image patches under the guidance of edge-preserved images. However, sometimes the values in homogeneous areas are inconsistent. In addition, the frequency information of image edges are exploited for defocus estimation, using spectrum contrast [27] or sub-band decomposition [28].

Interestingly, while the concept of the defocus map is closely related to bokeh, most existing methods neglect its applications in bokeh rendering. In our work, we show that the defocus map is an essential component for realistic bokeh rendering. It not only helps layered rendering, but also guides the image fusion in our rendering framework.

2.2. Shallow Depth of Field

Shallow DoF can be applied to autofocus systems [29, 30, 31, 32], bokeh synthesis from mobile phone camera [3, 5], and even supervision for monocular depth estimation [33, 34]. In addition, shallow DoF is implemented in video deblurring from a defocused video pair [35]. While a depth video and an all-in-focus video are generated from the defocused pair, we render shallow DoF from an all-in-focus image without the guidance of a depth map.

Among early methods [6, 36, 37, 38], ray tracing methods [6, 36, 38] can precisely reproduce the in-camera physical ray integration. However, they are computationally difficult to solve. Alternatively, accumulation buffer [37] is proposed to render a set of sub-apertures and to accumulate each sub-aperture view. Yet, this method is still time-consuming.

Large computational cost of physically based methods has prompted a search for a method to generate blur directly in the image domain. Some methods are therefore introduced to allow users to control focus parameters and blur amount [4, 5]. Wang *et al.* [5] propose a multi-stage model that combines real data and synthetic data to synthesize a shallow DoF effect from a single image. Wadhwa *et al.* [3] focus on the shallow DoF effect with dual-pixel sensors in the mobile phone camera by segmenting portraits/objects and predicting depth. In addition, a blending method for depth-based bokeh rendering [4, 32, 39] is proposed to generate the shallow DoF based on composition of images blurred by different kernels. The blur kernel can be produced by a scatter [40] or a cluster [41] operation. Moreover, Ignatov *et al.* [1] present a large-scale bokeh dataset and propose a multi-level network to gradually refine low-level details. Xiao *et al.* [42] synthesize physically plausible defocus blur for head-mounted displays in real-time. However this method requires a single RGB-D image as input.

To generate realistic bokeh, we apply a layered rendering idea inspired by [4]. The rendered results are fused with predicted radiance maps manually set in HDR to attain CoC effects, resulting in better visual quality.

2.3. Image Fusion/Blending

Image blending is widely used and refers to a certain region of a source image seamlessly replaces a certain area of a target image. As comparison, image fusion refers to extracting and then combining the most significant information from multiple images, and the generated fused single image is expected to be more informative for following applications, such as multi-focus fusion [43, 44], visible and infrared image fusion [45, 46], and medical

image fusion [47, 48].

Image blending aims to achieve smooth transition between the source and the target image. Alpha blending [49] is a simple and fast solution, however, it is too naive and blurs details in blending. A multi-scale blending algorithm [50] is put forward to blend images on different scales of Laplacian Pyramids. Gradient-based methods [51, 52, 53, 54] are commonly used. Perez *et al.* [51] first integrate a Poisson equation in blending. Farbman *et al.* [55] introduce a coordinate-based approach to improve speed by avoiding solving a large linear system. This method is made faster by implementing convolutions [56]. A general framework of image fusion is proposed to evaluate performances on multi-scale transform and sparse representation [57]. Zhang *et al.* [58] propose a Poisson blending loss and jointly optimize style as well as content. However this method optimize one image at a time, and the optimization process is time-consuming.

To maintain sharp in-focus areas and seamlessly blend blurred images and original images, we propose a novel image fusion designated for bokeh rendering. We first predict a initial mask from the predicted defocus map, then we implement the Poisson gradient loss in [58] and integrate it in our deep image blending.

3. Defocus to Focus Framework

Bokeh rendering conventionally requires three components: (i) depth relations, (ii) the focal plane, and (iii) out-of-focus rendering. In this paper, we propose a Defocus to Focus (D2F) fusion framework to implement the three components. In particular, D2F simplifies (i) and (ii) into defocus hal-

lucination, which integrates depth estimation and focal distance detection. The imagined defocus map can be a useful cue implying the blur amount of bokeh. For efficiency consideration, defocus hallucination is executed at half of the original image resolution.

For realistic out-of-focus rendering, we first introduce radiance virtualization into D2F to simulate transformation from image intensity to scene radiance, inspired by the fact that the real optical rendering in the DSLR camera is based on scene radiance [59]. The radiance map is manually set in HDR to increase the visibility of CoC. Given the low-resolution defocus map and the radiance map as weight, we next fuse images blurred by different kernels to generate bokeh, where a soft blur kernel helps the generating process achieve the CoC in a layer-wise manner.

Finally, to recover rendered results to the original resolution, we resort to a fusion strategy to ensure clear refocused regions determined by the defocus map and restrained by Poisson gradient loss. We adopt image fusion because we find that in-focus regions tend to be blurred due to naive upsampling. In summary, D2F consists of 3 modules: defocus hallucination, weighted layered rendering, and deep Poisson fusion. The pipeline is shown in Fig. 2. In what follows, we explain each module in detail. The notations of all parameters are listed in Table 1. We describe the algorithm in Alg 1.

3.1. Defocus Hallucination

Defocus hallucination estimates a defocus map. We highlight ‘hallucination’ instead of ‘estimation’ because the defocus map is ‘imagined’ conditioned on the blur kernels, rather than learning from supervision. Since the defocus map is another form of the depth map in depth prediction [33],

TABLE 1
 NOTATIONS OF PARAMETERS. THE SUBSCRIPT l MEANS THE LAYER l

Notation	Remark
\mathcal{I}_{hr}	All-in-focus RGB image of the original size
\mathcal{I}_{lr}	Low-resolution all-in-focus RGB image
\mathbf{D}_d	Disparity map
f	Disparity of the focal plane
\mathbf{D}	Defocus map
\mathcal{R}_0	Radiance map
\mathbf{M}_h	Mask of pixels in HDR
\mathbf{R}	Radiance map in HDR
r_l	The blur radius
\mathbf{M}_l	Mask of a defocus layer
\mathcal{I}_l	RGB image of a defocus layer
$\mathbf{K}(r_l)$	The blur kernel of a defocus layer
\mathcal{B}_l	Rendered result of a defocus layer
\mathcal{B}	Result of a layered rendering pipeline [4]
\mathcal{R}_r	Rendered radiance map
\mathcal{R}'_r	Rendered multiplication of radiance map and RGB image
\mathbf{M}_b	Initial binary Mask of fusion
\mathcal{B}_t	Target bokeh of deep Poisson network
\mathcal{B}_{up}	Upsampled bokeh from bilinear interpolation
\mathcal{B}_{lr}	Low-resolution bokeh
\mathbf{M}_s	Mask of deep Poisson fusion
\mathcal{B}_{hr}	Final rendered bokeh
\mathbf{D}_m	Multi-channel defocus map

any monocular depth estimation network can be used in implementation. In particular, we use a well-established architecture [60].

In contrast to the previous use of the defocus map [13, 14], we learn the defocus map in an unsupervised manner: a bokeh-free RGB image is used as input, and a single-channel defocus map is output by regression. We show that, even without supervision, the defocus map still can be predicted reasonably due to the latter implicit supervision.

Algorithm 1: The algorithm used in D2F.

Input: All-in-focus RGB image I_{hr} , Maximum weight of bright pixels α , Degree of difference among pixels β , Transition smoothness γ , Depth layers L , Blur kernel size function c , Defocus hallucination network f_d , Radiance virtualization network f_r , Layered rendering function f_l , Mask prediction network f_p , Bilinear resize function $Resize$

Output: Final rendered bokeh B_{hr}

- 1: $I_{lr} = Resize(I_{hr})$
 - 2: $\mathbf{D} = f_d(\mathcal{I}_{lr})$
 - 3: $\mathbf{R}_0 = f_r(\mathcal{I}_{lr})$
 - 4: $\mathbf{M}_h = |\mathcal{I}_{lr}| < 0.99$
 - 5: $\mathcal{R} = \mathbf{M}_h \cdot \alpha \mathcal{I}_{lr}^\beta + (1 - \mathbf{M}_h) \cdot \mathbf{R}_0$
 - 6: $\mathcal{R}'_r = f_l(\mathcal{R} \cdot \mathcal{I}_{lr}, \mathbf{D})$
 - 7: $\mathcal{R}_r = f_l(\mathcal{R}, \mathbf{D})$
 - 8: $\mathcal{B}_{lr} = \frac{\mathcal{R}'_r}{\mathcal{R}_r}$
 - 9: $\mathbf{M}_s = f_p(\mathcal{I}_{hr}, \mathbf{D})$
 - 10: $\mathcal{B}_{up} = Resize(\mathcal{B}_{lr})$
 - 11: $\mathcal{B}_{hr} = \mathbf{M}_s \cdot \mathcal{I}_{hr} + (1 - \mathbf{M}_s) \cdot \mathcal{B}_{up}$
-

As aforementioned, defocus hallucination integrates monocular depth estimation and focal plane detection. The defocus map \mathbf{D} takes the form

$$\mathbf{D} = \mathbf{D}_d - b(f), \quad (1)$$

where \mathbf{D}_d is the disparity map, f denotes the disparity of the focal plane, and $b(\cdot)$ is a broadcasting function that expands the singleton. In following equations, we neglect $b(\cdot)$ to simplify the notation.

Formally, defocus hallucination defines a function f_d such that

$$\mathbf{D} = f_d(\mathcal{I}_{lr}), \quad (2)$$

where $\mathcal{I}_{lr} \in \mathbb{R}^{\frac{H}{2} \times \frac{W}{2} \times 3}$ is the low-resolution all-in-focus RGB image. H and W are the height and width of the high-resolution input \mathcal{I}_{hr} . With the intermediate defocus map, we integrate it with the following radiance virtualization and layered rendering to simulate physically based bokeh rendering. Furthermore, defocus hallucination is the guidance of deep Poisson fusion for generation of the fusion mask.

3.2. Weighted Layered Rendering

3.2.1. Radiance Virtualization

In real photography, shallow DoF is generated from scene radiance rather than image intensity [6]. Therefore, we introduce radiance virtualization to transform raw RGB values into radiance. In addition, CoC is an important feature in realistic bokeh rendering and is closely related to radiance in HDR. To generate the CoC in color rendering, digital cameras typically have two rendering pipelines: i) the *photofinishing* model that adopts different imaging modes, and ii) the *slide or photographic reproduction* model that uses fixed color rendering [61]. Here we suppose that all images are captured in the latter mode and that the radiance of each pixel only depends on its RGB values. We apply layered rendering on scene radiance instead of image intensity, so we assign pixels with different weights according to their RGB values to establish the transformation from RGB values to scene radiance. As shown in Fig. 2, we use a network to compute scene radiance from RGB values and to predict the radiance map as

$$\mathbf{R}_0 = f_r(\mathcal{I}_{lr}), \quad (3)$$

where f_r is a network consisting of four convolution layers. The network outputs $\mathbf{R}_0 \in \mathbb{R}^{\frac{H}{2} \times \frac{W}{2}}$, which is considered an ‘imagined’ radiance map.

In addition, we observe that some bright pixels whose R, G, or B value is close to the upper bound, i.e., 255. These pixels are supposed to have larger weights indicating their actual energies than other pixels. A straightforward solution is to use the HDR operator. With HDR, the CoC effect can be enhanced in theory. However, in practice we find that designing a network to perform HDR is not needed, for a simple extension in the range of the radiance map is sufficient. Therefore, we deal with these bright pixels separately and allocate large weights to them as

$$\mathcal{R} = \mathbf{M}_h \cdot \alpha \mathcal{I}_{tr}^\beta + (1 - \mathbf{M}_h) \cdot \mathbf{R}_0, \quad (4)$$

where \cdot is the element-wise product, $\mathcal{R} \in \mathbb{R}^{\frac{H}{2} \times \frac{W}{2} \times 3}$ is the modulated radiance map, and $\mathbf{M}_h \in \mathbb{R}^{\frac{H}{2} \times \frac{W}{2}}$ is a mask which denotes whether R, G, or B value of each pixel is more than a threshold. α and β are two hyperparameters, where α controls the maximum weight of bright pixels, and β adjusts the degree of difference among RGB color channels. From experiments, one can see that this operation leads to a similar HDR effect. We remark that radiance virtualization is essential: empirically training defocus hallucination alone without radiance virtualization can lead to non-convergence of the network sometimes. A plausible explanation is that the radiance map also provides some form of supervision to defocus hallucination.

3.2.2. Layered Rendering

The physically motivated refocusing pipeline proposed in SteReFo [4] can mimic the real rendering process efficiently. The core idea is to decompose the scene into different depth layers and fuses them after blurring each layer with pre-defined blur kernels conditioned on a known focus plane.

Given a defocus map $\mathbf{D} \in \mathbb{R}^{\frac{H}{2} \times \frac{W}{2}}$, we quantize the depth values into L depth layers. Thus, the blur radius of the l -th layer $r_l \in \mathbf{r}$, $\mathbf{r} \in \mathbb{R}^L$, $l = 1, \dots, L$, can be computed by

$$r_l = c(l), \quad (5)$$

where $c(\cdot)$ is a camera-dependent function which allocates the corresponding blur kernel size w.r.t. l . In D2F we define $c(\cdot)$ as a piecewise linear function, because the depth of each layer is considered uneven. From the defocus map \mathbf{D} , the l -th layer of the image \mathcal{I}_{lr} is generated by

$$\mathcal{I}_l = \mathbf{M}_l \cdot \mathcal{I}_{lr}, \quad (6)$$

where $\mathbf{M}_l = \mathbb{1}(|\mathbf{D} - \frac{l}{L}| < \frac{1}{L})$. In implementation the indicator function $\mathbb{1}(\cdot)$ is replaced with a smooth function according to [4] as

$$\mathbf{M}_l = \frac{1}{2} + \frac{1}{2} \tanh \left(\gamma \left(\frac{1}{L} - |\mathbf{D} - \frac{l}{L}| \right) \right). \quad (7)$$

The value of γ defines the smoothness of transition between layers. On the one hand, a smaller value tends to highlight the gap between each layer and make the final fused result more fragmented. On the other hand, a larger

value would fade the CoC. Thus $\mathcal{I}_l \in \mathbb{R}^{\frac{H}{2} \times \frac{W}{2} \times 3}$ is blurred as

$$\mathcal{B}_l = \mathbf{K}(r_l) * \mathcal{I}_l, \quad (8)$$

where $\mathcal{B}_l \in \mathbb{R}^{\frac{H}{2} \times \frac{W}{2} \times 3}$ is the bokeh result of layer l , and $\mathbf{K}(r_l) \in \mathbb{R}^{r_l \times r_l}$ is the blur kernel conditioned on the kernel size r_l . Given the rendered \mathcal{B}_l 's, fusing them back takes the form

$$\mathcal{B} = \frac{\sum_{l=1}^L \mathcal{B}_l \prod_{j=l+1}^L (1 - \mathbf{M}_j)}{\sum_{l=1}^L (\mathbf{K}(r_l) * \mathbf{M}_l) \prod_{j=l+1}^L (1 - \mathbf{M}_j)}, \quad (9)$$

where \mathbf{M}_{L+1} is a zero matrix. $l = 1$ is considered no blur in Eq. (8), so $\mathcal{B}_1 = \mathcal{I}_1$.

We combine Eq. (6) (7) (8) (9) to define layered rendering as function f_l such that

$$\mathcal{B} = f_l(\mathcal{B}_l, \mathbf{M}_l) = f_l(\mathcal{I}_l, \mathbf{D}), \quad (10)$$

By integrating layered rendering with defocus hallucination and radiance virtualization, one can attain visually pleasing CoC effects. Concretely, our design choices are:

- i) *Generating soft blur kernels.* To generate the realistic disk-like CoC, we design a soft disk blur kernel instead of a hard one formed by 0 or 1. For a blur kernel $\mathbf{K}(r_l)$, the value of a hard kernel follows

$$k_h(x, y, r_l) = \begin{cases} 0, & \text{if } r_l^2 - x^2 - y^2 < 0 \\ 1, & \text{otherwise} \end{cases}, \quad (11)$$

where x and y indicate the horizontal and vertical distance relative to the

center of the blur kernel. Note that, this function is not differentiable, a smooth approximation [4] can replace as

$$h(z) = \frac{1}{2} + \frac{1}{2} \tanh(z). \quad (12)$$

Following Eq. (12), we define the value in a soft disk kernel by

$$k_s(x, y, r_l) = \frac{1}{2} + \frac{1}{2} \tanh\left(\sigma(r_l^2 - x^2 - y^2) + \varphi\right), \quad (13)$$

where σ and φ control the shape of the disk kernel. The comparison of hard and soft kernels with different sizes is shown in Fig. 3. One can see that the soft kernel looks more like a disk than the hard one, especially when the kernel size is small. This creates a natural CoC effect. Therefore, D2F uses $k_s(\cdot, \cdot, \cdot)$ to implement $\mathbf{K}(r_l)$.

- ii) *Customizing blur kernel sizes.* We find that the blur amount of the bokeh image is unbalanced during weighted layered rendering, where a small blur amount tends to appear for most layers in a defocus map. Therefore, we set the intervals of pre-defined kernel sizes in a non-uniform manner. Specifically, we define that $c(\cdot)$ as a piecewise linear function in Eq. (5) such that

$$c(l) = \begin{cases} 2 * l + 1, & 1 \leq l < 3 \\ 4 * (l - 3) + 7, & 3 \leq l < 8 \\ 6 * (l - 8) + 27, & 8 \leq l < 11 \\ 8 * (l - 11) + 45, & 11 \leq l < 15 \end{cases}. \quad (14)$$

$l = 1$ can be considered no blur.

- iii) *Modulating blur with the defocus map and the radiance map.* In D2F we

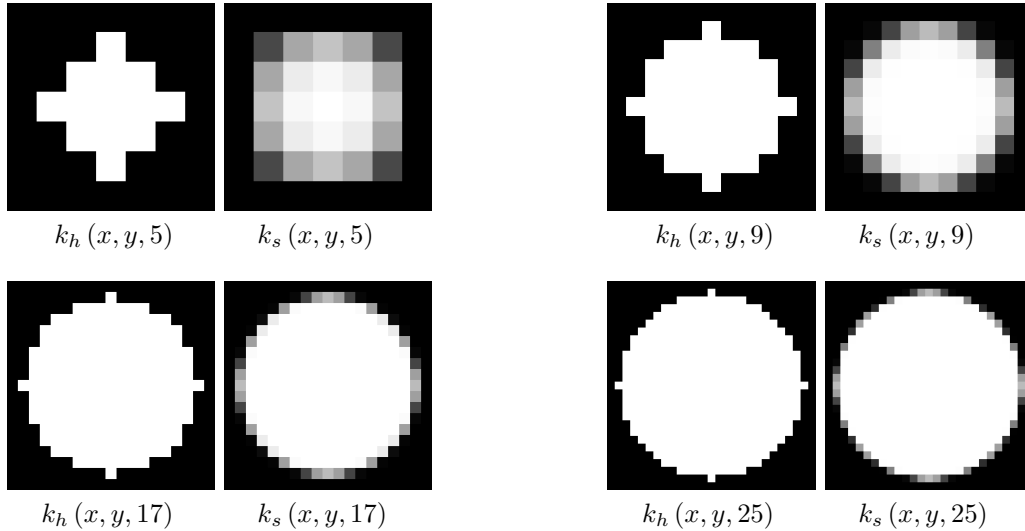


Figure 3. Visualizations of hard (left) and soft (right) disk blur kernels with different kernel sizes. Visualizations of hard disk blur kernels $k_h(x, y, r_l)$ and soft disk blur kernels $k_s(x, y, r_l)$ with different kernel sizes.

propose to use the predicted defocus map \mathbf{D} and the radiance map \mathcal{R} to further modulate blur and to increase the reality of bokeh. We render the radiance map and multiplication of the radiance map and the RGB image separately under the guidance of \mathbf{D} , which outputs \mathcal{R}_r and \mathcal{R}'_r . \mathcal{R}'_r divided by \mathcal{R}_r is the rendered bokeh. Such modulation slightly modifies Eq. (10) to

$$\mathcal{B}_{lr} = \frac{\mathcal{R}'_r}{\mathcal{R}_r}, \quad (15)$$

where

$$\begin{aligned} \mathcal{R}'_r &= f_l(\mathcal{R} \cdot \mathcal{I}_{lr}, \mathbf{D}) \\ \mathcal{R}_r &= f_l(\mathcal{R}, \mathbf{D}) \end{aligned} \quad (16)$$

Here we add the subscript to \mathcal{B} to remind that the generated bokeh is at

low resolution. \mathcal{R}'_r integrates the radiance map in bokeh rendering, which helps to produce the CoC. It is worth mentioning that layered rendering does not require training, and the formulation of the radiance map and the defocus map is learned. The rendering of the radiance map is introduced to ensure consistency in tones between \mathcal{I}_{lr} and \mathcal{B}_{lr} . $f_l(\mathcal{R}, \mathbf{D})$ acts as a normalizer of weighted layered rendering $f_l(\mathcal{R} \cdot \mathcal{I}_{lr}, \mathbf{D})$, because we introduce the production of the radiance map and the original image, and this step might change the overall brightness. As shown in Fig. 4, this normalization improves the quality of the rendered bokeh. In the second column, the rendered bokeh without normalization produces artifacts in areas which are supposed to be consistent in color. If we add normalization and render bokeh as the third column, the color inconsistency is eliminated.

3.3. Deep Poisson Fusion

Since the rendered low-resolution bokeh \mathcal{B}_{lr} needs to be recovered to the original size, we expect to find an appropriate upsampling approach. Super-resolution or other learning-based methods [5, 62] can be employed to increase the resolution of bokeh. However, these approaches tend to destroy the CoC effect. Naive upsampling methods such as bilinear upsampling can also fail to render realistic bokeh because they blur the whole low-resolution image including the in-focus regions. One may consider computing a binary mask from the defocus map to keep the clearness of the in-focus region, but we find this creates unpleasant artifacts around boundaries. Next we show how we deal with the boundary artifacts.

We implement the predicted defocus map as guidance for the fusion mask. Therefore, an expected fusion pipeline defines a function f_p that generates a



Figure 4. Qualitative results with or without normalization.

soft mask $\mathbf{M}_s \in \mathbb{R}^{H \times W}$, defined by

$$\mathbf{M}_s = f_p(\mathcal{I}_{hr}, \mathbf{D}). \quad (17)$$

To predict \mathbf{M}_s , a loss function is used for fusing high-resolution small-aperture images and the upsampled rendered bokeh. Inspired by Poisson blending loss [58], the Poisson gradient loss is applied to force the gradient consistency of the in-focus region for both large-aperture images $\mathcal{B}_{hr} \in \mathbb{R}^{H \times W \times 3}$ and small-aperture images $\mathcal{I}_{hr} \in \mathbb{R}^{H \times W \times 3}$. The loss function takes the form

$$L_p(\mathcal{B}_t, \mathcal{B}_{hr}) = \frac{1}{2HW} \sum_{m=1}^H \sum_{n=1}^W [\nabla \mathcal{B}_t - \nabla \mathcal{B}_{hr}]_{mn}^2, \quad (18)$$

where $\mathcal{B}_{hr} = \mathbf{M}_s \cdot \mathcal{I}_{hr} + (1 - \mathbf{M}_s) \cdot \mathcal{B}_{up}$ is the final fusing result. \mathcal{B}_t represents the target image and is defined by

$$\mathcal{B}_t = \mathcal{I}_{hr} \cdot \mathbf{M}_b + \mathcal{B}_{up} \cdot (1 - \mathbf{M}_b), \quad (19)$$

where ∇ indicates the Laplacian gradient operator. $\mathcal{B}_{up} \in \mathbb{R}^{H \times W \times 3}$ is generated from \mathcal{B}_l by bilinear upsampling. $\mathbf{M}_b \in \mathbb{R}^{H \times W}$ is a binary mask converted from the defocus map using a threshold θ such that, for any position (x, y) , $\mathbf{M}_b(x, y) = 1$ if $\mathbf{D}(x, y) \geq \theta$, and $\mathbf{M}_b(x, y) = 0$ if $\mathbf{D}(x, y) < \theta$. We integrate the defocus map in our fusion framework as Eq. (19) to guide the deep Poisson network.

3.4. Loss Function

The training of the network is divided into two stages. The first stage jointly trains defocus hallucination and radiance virtualization, while the

second stage trains deep Poisson network. Layered rendering does not require training.

The loss for defocus hallucination and radiance virtualization is defined by

$$L_{stage1} = L_1(\mathcal{B}_{hr}, \mathcal{B}_{gt}) + \lambda \cdot L_{vgg}(\mathcal{B}_{hr}, \mathcal{B}_{gt}) + L_{ssim}(\mathcal{B}_{hr}, \mathcal{B}_{gt}) + \delta \cdot L_{grad}(\mathbf{D}, \mathcal{I}_{lr}), \quad (20)$$

where L_1 is the ℓ_1 loss, L_{vgg} is the perceptual loss based on the pre-trained VGG19 [63], and L_{ssim} is the structural similarity (SSIM) loss [64]. L_{grad} is the pyramid gradient loss used to constrain the defocus map to be locally smooth, especially in the areas with consistent colors. L_{grad} takes the form

$$L_{grad}(\mathbf{D}, \mathcal{I}_{lr}) = \frac{1}{S} \sum_{i=1}^S \left(|\partial_x \mathbf{D}^i| \cdot e^{-\|\partial_x \mathcal{I}_{lr}^i\|_1} + |\partial_y \mathbf{D}^i| \cdot e^{-\|\partial_y \mathcal{I}_{lr}^i\|_1} \right), \quad (21)$$

where S denotes the the number of scales.

For training deep Poisson network, we further add the poisson gradient loss to Eq. (20) as

$$L_{stage2} = L_{stage1} + \zeta \cdot L_p(\mathcal{B}_t, \mathcal{B}_{hr}). \quad (22)$$

The Poisson gradient loss adds gradient constraints to in-focus areas, as in Fig. 2.

3.5. Implementation Details

We implement our method based on PyTorch. The hardware platform includes a single Nvidia GTX 1080 GPU with 256 GB RAM and Intel Xeon processor. To accelerate the inference speed, we use ResNeXt50 [65] pre-trained on ImageNet [66] as the backbone in defocus hallucination. In Eq. (4), empirically $\alpha = 3$ and $\beta = 5$, because we want to widen the difference between bright pixels that are considered in HDR and other pixels. The threshold θ used to generate \mathbf{M}_b is set to 0.25, because we find that the threshold does not have a decisive effect on the generated bokeh. In Eq. (7), $\gamma = 100$, because a smaller value tends to highlight the gap between each layer and make the result more fragmented, and a larger value would fade the CoC. In Eq. (13), $\sigma = 0.25$ and $\varphi = 0.5$, because under this setting, the blur kernel resembles a smooth disk. In Eq. (20), λ is set to 0.1 because we want to keep $L_1(\cdot, \cdot)$, $L_{vgg}(\cdot, \cdot)$, and $L_{ssim}(\cdot, \cdot)$ on the same order of magnitude at the beginning of training. δ is set to 0.1, so it is enough to restrain the gradient of defocus map while maintaining the quality of generated bokeh. The number of scale S in the pyramid gradient loss is set to 4. In Eq. (22), ζ is set to 10, so it is enough to ensure the sharpness of in-focus regions.

4. Results and Discussions

In this section, we first introduce the experimental setting. Then we report the quantitative and qualitative performance of D2F on a large-scale bokeh dataset EBB!. Finally, we conduct an ablation study to analyze the influence of different factors on bokeh.

4.1. Dataset and Experimental Setup

Everything is Better with Bokeh! (EBB!) [1] is a large-scale dataset consisting of 4694 aligned wide/shallow depth-of-field image pairs captured using the Canon 7D DSLR with 50mm f/1.8 lenses. EBB! is initially proposed for the AIM 2020 Rendering Realistic Bokeh Challenge [67]. The purpose of this challenge is to achieve the shallow depth-of-field with the best perceptual quality similar to the ground truth as measured by the Mean Opinion Score (MOS). MOS is defined as a numeric value ranging from 1 to 5 (5 - comparable perceptual quality, 4 - slightly worse, 3 - notably worse, 2 - poor perceptual quality, 1 - completely corrupted image) [67]. For evaluation, we divide the dataset into a training set with 4224 pairs and a validation set with 470 pairs, which is termed as Val470. The training process includes two stages. At the first stage, we jointly train the defocus hallucination module and the radiance virtualization module on the 512×512 image resolution; at the second stage, we train the deep Poisson fusion alone on the original 1024×1024 resolution.

In experiments, we use the peak signal to noise ratio (PSNR) and structural index similarity (SSIM) for evaluation. PSNR and SSIM are two widely used metrics in image quality assessment. In addition, MOS is the quantitative criterion in AIM 2020 Rendering Realistic Bokeh Challenge.

4.2. Comparison With State of the Art

4.2.1. Quantitative Results

D2F is initially proposed to participate in the AIM 2020 Rendering Realistic Bokeh Challenge [67] and our solution is the runner-up of all methods.

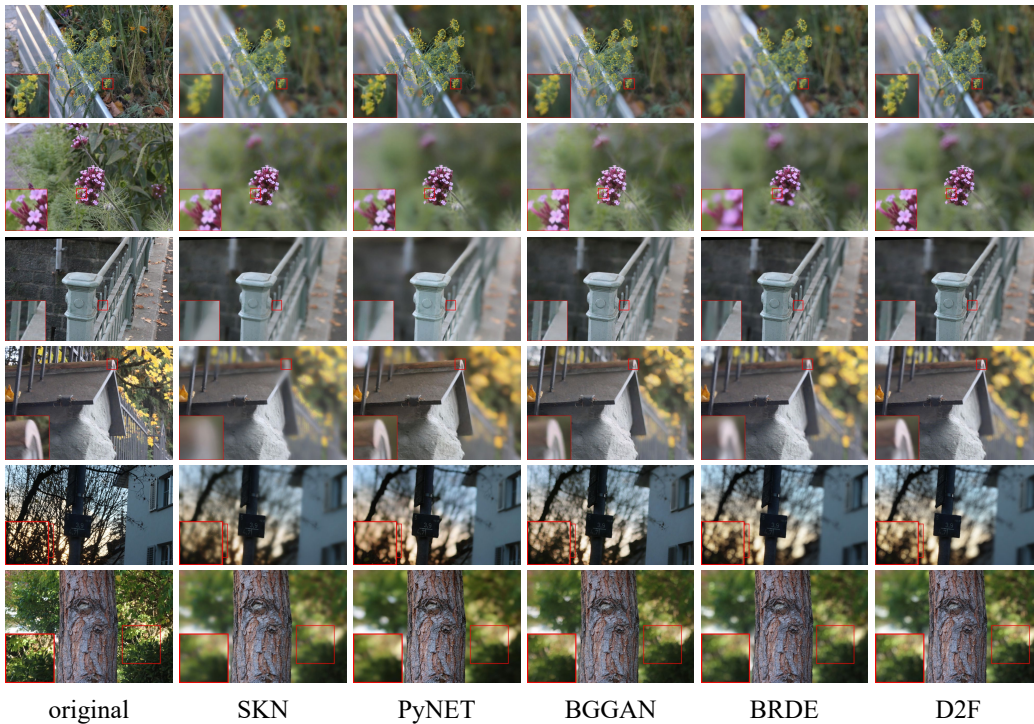


Figure 5. **Visual results obtained with four different methods.** From left to right: the original narrow aperture image, SKN(Selective Kernel Networks for Bokeh Effect Simulation) which ranked fourth from Track 1 of AIM 2019 Challenge on Bokeh Effect Synthesis [68], PyNET [1], BGGAN [69], our previous naive solution [2], and our current gradient-based fusion solution. In the first four rows, D2F achieves better results than our previous solution [2], and D2F is competitive among other methods. In addition, in the last two rows, D2F obtains prominent CoC compared with other methods.

TABLE 2
 QUANTITATIVE RESULTS FROM THE AIM 2020 RENDERING REALISTIC BOKEH CHALLENGE. RESULTS ARE SORTED BASED ON THE MOS SCORES. OUR CURRENT METHOD D2F AND OUR PREVIOUS METHOD ARE IN THE LAVENDER ROWS. THE BEST PERFORMANCE IS IN BOLDFACE

Team	MOS	PSNR	SSIM
BGGAN [69]	4.2	23.58	0.8770
PyNET [1]	–	23.28	0.8780
SKN [68]	–	23.18	0.8851
Dutta <i>et al.</i> [39]	–	22.14	0.8633
D2F	–	23.11	0.8862
BRDE [2]	4.0	22.94	0.8842
CET_SP [67]	3.3	21.91	0.8201
CET_CVLab [67]	3.2	23.05	0.8591
TeamHorizon [67]	3.2	23.27	0.8818
IPCV_IITM [67]	2.5	23.77	0.8866
CET21_CV [67]	1.3	22.80	0.8628
CET_ECE [67]	1.2	22.85	0.8629

In the competition, we apply a naive alpha blending approach for upsampling [2].

Table 2 shows the performance of our model. We compare results from AIM 2019 Rendering Realistic Bokeh Challenge [68] as well as AIM 2020 Rendering Realistic Bokeh Challenge. It is worth mentioning that we send our new result to the organizers and get PSNR and SSIM results, however, the corresponding MOS result is unlikely to obtain because it is from a user study that is already finished. As shown in Table 2, D2F with deep Poisson fusion achieves better results than our previous method [2] in terms of PSNR and SSIM, and our previous method ranks second in AIM 2020 Rendering Realistic Bokeh Challenge. Although we are not able to compare D2F with methods from AIM 2020 Rendering Realistic Bokeh Challenge on MOS, we provide qualitative results to show that D2F is superior to our previous work.

TABLE 3
 RUNTIME OF DIFFERENT METHODS ON GPU

	SKN [68]	D2F	PyNet [1]
Time(s)	0.87	0.58	0.24

4.2.2. Qualitative Results

In this section, we compare D2F to the state-of-the-art solutions [68, 1, 69] that were trained and tuned specifically for bokeh rendering. The visual results of all methods are presented in Fig. 5. As shown in Fig. 5, D2F shows competitive results in producing CoC. In addition, D2F achieves better quality compared with the previous naive blending method, because the manual threshold of naive blending sometimes does not fit the minimum value of defocus map, in which case the naive blending results have a small clear area, even none. Implementing Poisson blending solves this issue.

4.2.3. Runtime

In this section we compute time in ms of different methods on GPU. The result is shown in Table 3.

4.3. Ablation Study

As mentioned above, our model consists of different components and is trained in a multi-module manner with the combination of different losses and multiple blur kernels. Therefore, we conduct an ablation study to compare different settings and demonstrate the effectiveness and superiority of D2F. Fig. 6 presents intermediate outputs which consist of defocus maps, weight maps, fusion masks, and the generated bokeh.

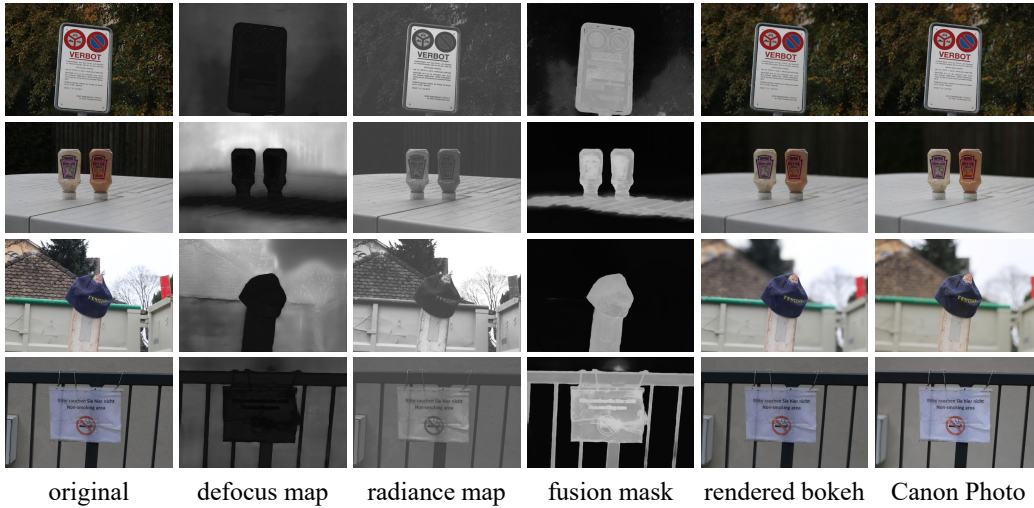


Figure 6. Visual results obtained with D2F. Best zoomed-in on screen.

TABLE 4
 QUANTITATIVE RESULTS OF DEFOCUS HALLUCINATION AND RADIANCE
 VIRTUALIZATION TRAINING WITH DIFFERENT LOSSES ON VAL470

Loss	PSNR	SSIM
L_{l1}	23.6241	0.8730
$L_{l1} + L_{grad}$	23.6202	0.8745
$L_{l1} + L_{ssim} + L_{grad}$	23.6780	0.8794
L_{total}	23.7091	0.8795

TABLE 5
 QUANTITATIVE RESULTS OF FUSION NETWORK TRAINING WITH DIFFERENT LOSSES
 ON VAL470

Loss	PSNR	SSIM
$L_{l1} + L_{Poisson}$	23.6605	0.8776
$L_{l1} + L_{ssim} + L_{Poisson}$	23.7123	0.8817
$L_{l1} + L_{ssim} + L_{vgg} + L_{Poisson}$	23.7298	0.8817
L_{total}	23.7342	0.8818

4.3.1. *Combination of Losses*

As shown in Table 4 and Table 5, we obtain the best results when all of the loss functions are used. Besides, we visualize some examples of the predicted defocus maps with different combinations of losses in Fig. 7 to verify the effect of each loss. One can see that the predicted defocus maps become more delicate on in-focus regions, smoother on out-of-focus regions, and more precise in terms of blurring amount by adding loss function gradually. The third column indicates that the gradient loss helps to generate consistent defocus maps with sharp discontinuities around in-focus objects such as the human (row 1), the sign (row 2) and the pole (row 3,4). If we add SSIM loss as the fourth column, the quality of defocus map is improved in background regions, and the shape of objects is better retained, such as the pole and the man. The fifth column shows that the perceptual loss helps to improve the overall quality of the defocus map, as the man, the sign and the pole are all intact, and the background is flattened. Particularly, we discovered that pyramid gradient loss in Fig. 7 is helpful for the training process to converge. Not only does pyramid gradient loss make the predicted defocus map more accurate, but also it improves the performance of generated bokeh.

4.3.2. *Settings of Blur Kernels*

The number and size of the blur kernels are largely determined by experience. On the one hand, too many kernels will slow down the running speed while too few kernels will cause a certain limitation. On the other hand, the maximum kernel size is supposed to be consistent with the maximum blur amount in a real scene. However, we observe that the defocus map corresponding to the large-scale blur is hard to learn as the blur amount varies



Figure 7. **Visualization of defocus maps.** The first row is all-in-focus image. The second row to the last row present the predicted defocus maps training with L_{l1} , $L_{l1}+L_{grad}$, $L_{l1}+L_{ssim}+L_{grad}$ and L_{total} , respectively.

greatly among the images and most of them have a small blur amount. In consequence, we choose to have more blur kernels with a small blur radius than those with a large blur radius. In addition, We conduct some experiments on the settings of blur kernels. We compare the different numbers and maximum sizes of blur kernels in Fig. 8. We chose 11, 13, 15, 17, and 19 kernels for ablation studies.

We adopt the 15-kernel solution in Eq. (14) according to the experiments. In addition, we choose the maximum kernel sizes to be 49, 59, 69, 79, and 89. We adopt the maximum kernel size to be 69 as Eq. (14) according to the experiment to achieve better PSNR and SSIM and occupy less memory. To generate a smooth bokeh result, the kernel size should be set continuously. We adopt two sampling strategies, i.e., growing sampling and uniform

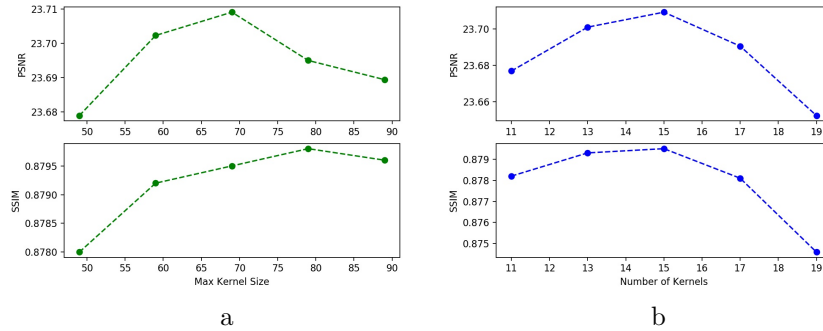


Figure 8. PSNR and SSIM results of different maximum kernel sizes and different number of kernels.

TABLE 6
 QUANTITATIVE RESULTS OF DIFFERENT SAMPLING STRATEGIES ON VAL470

	Growing	Uniform
PSNR	23.7091	23.5260
SSIM	0.8795	0.8628

sampling. The growing sampling is what we adopt in Section 3.2. For uniform sampling, the interval of kernel sizes is set to 4 from beginning to end. The comparison between the two strategies is shown in Table 6. The above analysis can help us set the pre-defined blur kernels better.

4.3.3. Radiance Module

As shown in Table 7, the model with radiance virtualization achieves better results with the model without radiance module quantitatively. The obtained radiance map can demonstrate scene radiance, which is more suitable for bokeh rendering than image intensity. To further prove this, we show some examples in Fig. 9 and Fig. 10, where we present differences with or without radiance relationship as well as the gap between radiance maps and



Figure 9. Qualitative results of gray images and radiance maps.

TABLE 7
 QUANTITATIVE RESULTS WITH OR WITHOUT RADIANCE VIRTUALIZATION, OR USING
 GRAY IMAGES AS RADIANCE GUIDANCE ON VAL470

	w/ Radiance	w/o Radiance	Gray image
PSNR	23.7091	23.6780	23.6527
SSIM	0.8795	0.8794	0.8774

gray images generated from RGB images.

In Fig. 9 we can distinguish between gray images and radiance maps which demonstrate scene radiance, and in Fig. 10 bokeh results from a radi-



Figure 10. Qualitative results of with or without radiance maps, or applying gray images.

ance map and a gray image are presented, we can conclude that a radiance map help produce CoC in the blurred out-of-focus regions with its revelation of radiance relationships between pixels, while bokeh obtained from a gray image or only an original RGB input fails to achieve distinctive CoC effects.

4.3.4. Fusion Methods

Our goal is to maintain the clearness of in-focus regions, and we adopt various fusion approaches to achieve our expectations. Our criteria can be divided into two parts: visual clearness of in-focus objects and overall PSNR and SSIM. In other words, we aim to reach better results quantitatively and qualitatively. In Table 8, we present six schemes. Naive blending represents the method applying in [2]. For Laplacian Pyramid blending, we generate the

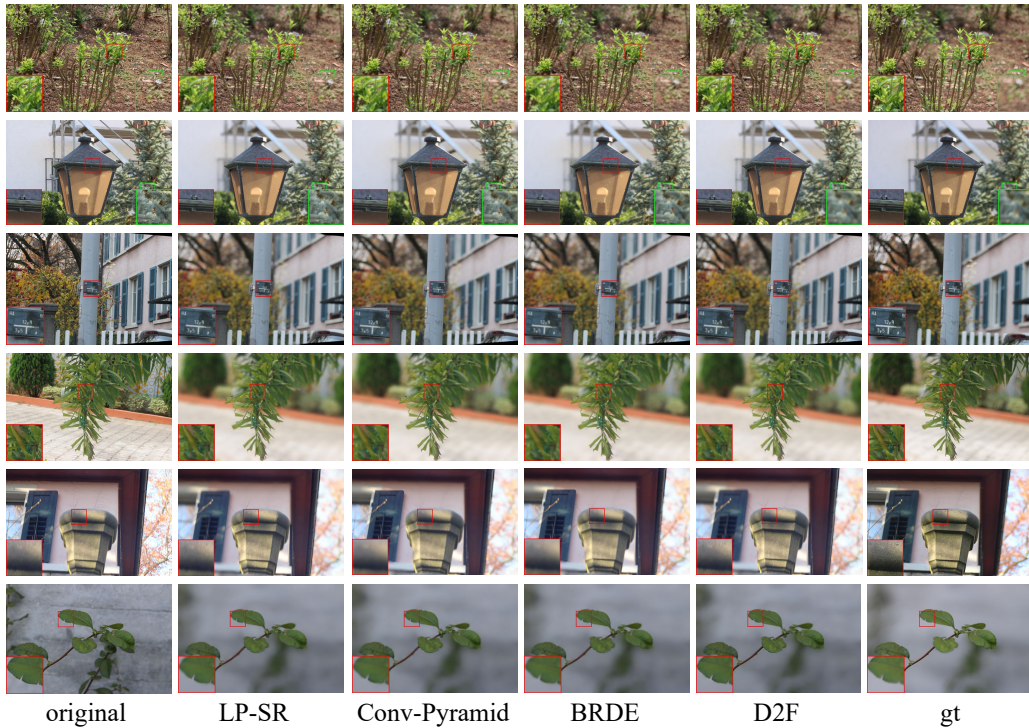


Figure 11. **Qualitative results of different fusion methods.** From left to right: the all-in-focus input, LP-SR [57], Conv-Pyramid [56], our previous solution [2], D2F and the ground truth. Green square and red square in each image represent respectively inconsistent blurring and blurred in-focus regions. Our method is the best solution compared to other approaches regarding the two standards.

mask in the same manner as naive blending. For naive Poisson blending, we transform defocus map into a binary mask, which is seen as input together with the original narrow-aperture image to produce blending results. As shown in implementation details, the threshold for transformation is set to 0.25, where any pixel with a defocus value larger than 0.25 is set to 0. In addition, we evaluate two recent fusion methods. One of the methods is based on multi-scale transform and sparse representation [57], and the other one is based on convolution pyramid blending(Conv-Pyramid) [56]. One can

TABLE 8
 QUANTITATIVE RESULTS OF DIFFERENT FUSION METHODS ON VAL470

Method	PSNR	SSIM
naive Poisson blending	23.3353	0.8708
Laplacian Pyramid	23.6455	0.8698
LP-SR [57]	23.6805	0.8713
BRDE [2]	23.7091	0.8795
Conv-Pyramid [56]	23.7247	0.8812
D2F	23.7342	0.8818

conclude from the quantitative results that our current fusion method which employs Poisson gradient constraint and deep neural network achieves the best results.

In Fig. 11, we compare different fusion schemes. We discovered that bilinear upsampling is invalid for maintaining the sharpness of in-focus regions. Naive Poisson blending can produce rather clear in-focus regions. However, as we provide a binary mask set empirically to the blending process, the whole image displays inconsistent blurring regions and performs poorly around edges. Laplacian Pyramid blending performs better than naive Poisson blending on defocused regions. However, it also fails to keep sharp edges. Our network is capable of generating the most pleasing blending results among these methods.

4.4. Training Strategy

We train our defocus hallucination module in a concise manner that the defocus hallucination network produces a single-channel defocus map on a resolution of 512×512 . Our deep Poisson network is trained on a resolution of 1024×1024 .

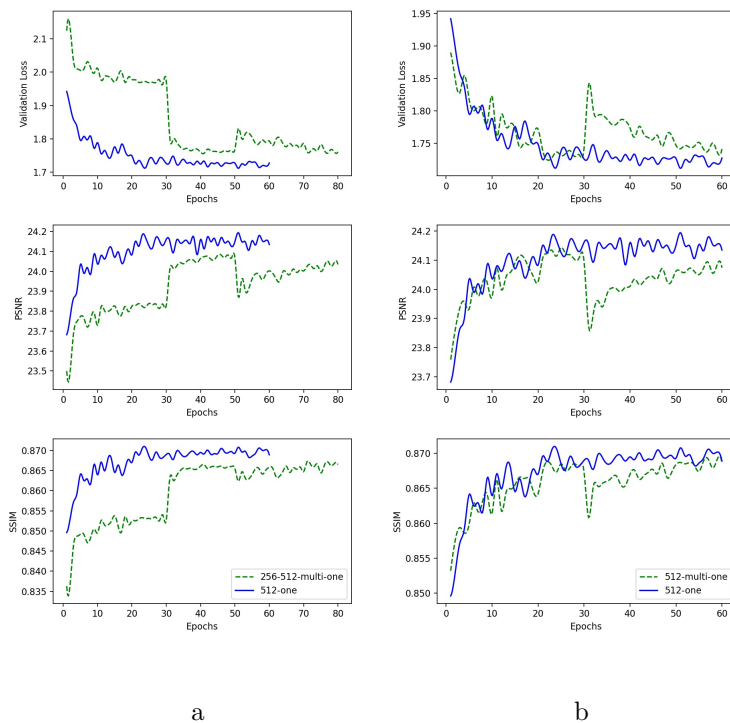


Figure 12. Validation loss and PSNR results of different training strategy. The blue line is our current strategy.

We compare our current defocus hallucination training scheme with two different strategies: i) our previous method [2], where the network is trained to produce a multi-channel defocus map on 256×256 for 30 epochs, finetuned on 512×512 for 20 epochs, and is trained to generate a single-channel defocus map on 512×512 with the parameters of radiance virtualization module and defocus hallucination module except for the last two convolutional layers fixed for 30 epochs, and ii) A two-stage training where the network first outputs a multi-channel defocus map on 512×512 to converge faster, and switches

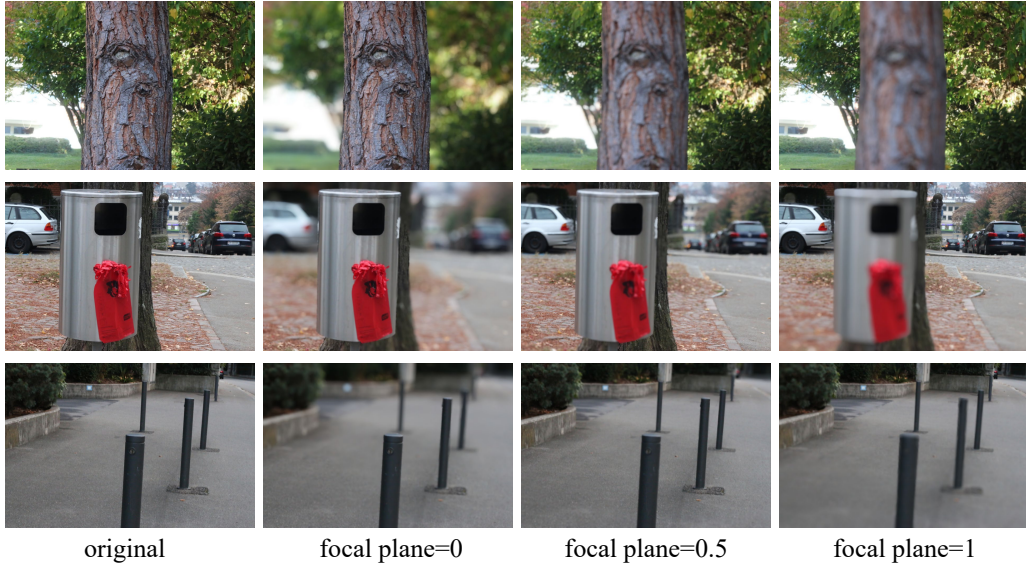


Figure 13. **Bokeh from different focal distances.** From column 2 to column 4, the focal plane is changed from foreground to background. We define the focal plane as the relative distance from the focused plane to the camera.

to produce the single-channel result. The multi-channel defocus map can be written as:

$$\mathbf{D}_m = f_m(\mathcal{I}_{lr}) \quad (23)$$

\mathbf{D}_m is the multi-channel defocus map which is normalized by softmax function, so it can also be considered as a probabilistic map. The channels of \mathbf{D}_m is set to 6, specifically. In order to generate single-channel results from multi-channel results, we replace the last convolutional layer and softmax layer with one convolutional layer that has a one-channel output.

As shown in Fig. 12, the blue line is our current strategy that train images on 512×512 and output single-channel defocus maps. In (a) the green line indicates our previous three-step training method. In this scheme we train the network to produce multi-channel defocus maps on 256×256 to converge

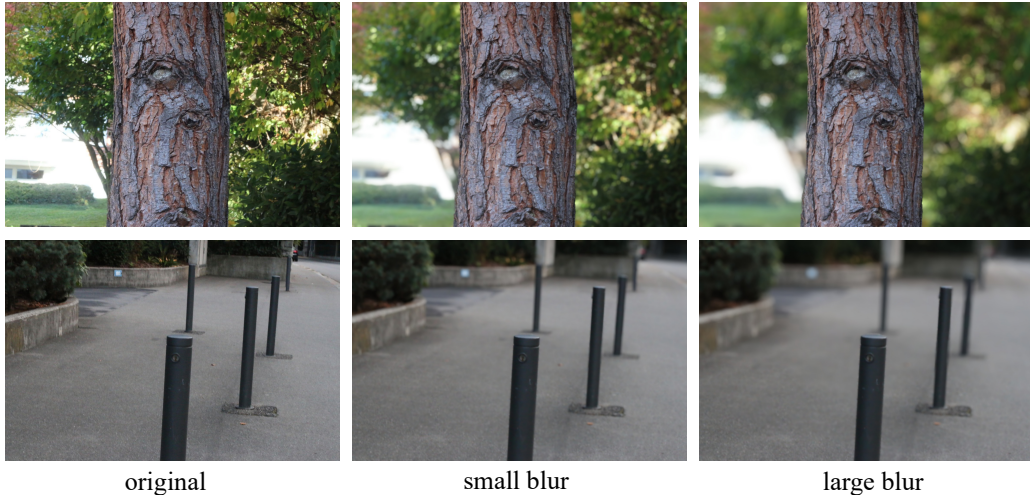


Figure 14. Bokeh with different blur amount.

faster, then we finetuned on 512×512 , finally, we switch to output single-channel defocus maps.

The green dotted line in table *b* is a two-step scheme that trains images on 512×512 , and the scheme is the same as the last two steps of the three-step strategy from table *a*. The sudden decline or rise in these two green dotted lines are resulted from changing training resolutions or the channels of output defocus maps. To achieve better CoC, we need to output single-channel defocus maps, so the last step of each scheme is the same.

Judging from the graph, the validation loss and the PSNR result of D2F are superior to those of our previous approach and another multi-stage training strategy which are originally designed to converge faster.

4.5. Applications

Since D2F is trained on a dataset where foreground objects are in-focus, we can assume the focal plane is at 0 in terms of relative depth. Therefore,

we can alter the defocus map in order to change the focal plane. As shown in Fig. 13, we set the relative disparity map from 0 to 1, and we focus on three planes where the focal distance is 0, 0.5 and 1. We define the focal distance as the relative distance from the focused plane to the camera, ranged from 0 to 1. In addition, we use pre-defined blur kernels, so we can also modify the blur amount by different blur kernel sizes, as shown in Fig. 14. It is worth mentioning that other methods from AIM 2019 Rendering Realistic Bokeh Challenge and AIM 2020 Rendering Realistic Bokeh Challenge are not able to adjust the focal plane and the blur amount.

4.6. Failure Case Analyses

Although D2F achieves pleasing bokeh effects, it still has some defects. We show some failure cases in this section. As shown in Fig. 15, some in-focus parts of the generated bokeh images are blurred by mistake. This phenomenon is caused by false defocus hallucination, and the defocus map might be inaccurate or not versatile enough because of our manual settings of blur kernels. The defocus map is likely to be inconsistent when the structure is too thin, such as the branches and fences in Fig. 15. In addition, as shown in the row 4 from Fig. 15, if the focused object has a stripe-like shape, it might get blurred with the surrounding background. We believe the introduction of depth map can improve the rendered result. If the depth map is accurate, it can provide with correct ordinal relationship between objects, so that D2F is able to distinguish in-focus and out-of-focus regions.

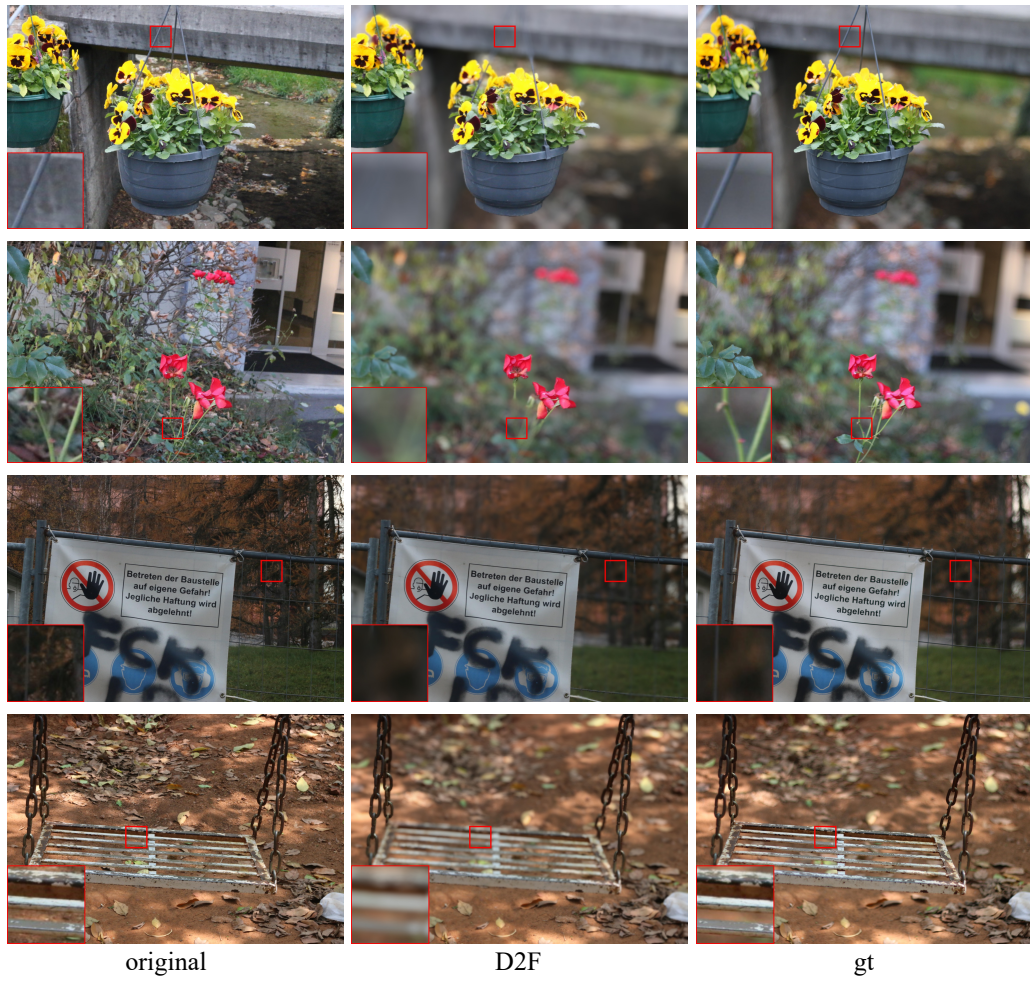


Figure 15. Examples of some failure cases.

5. Conclusion

We have presented an effective fusion framework D2F to predict a bokeh image from a single narrow aperture image. By introducing defocus hallucination within our network using only a bokeh image as supervision, we train our defocus hallucination network to produce a single-channel defocus map, improving the aesthetic quality of the synthesized bokeh. D2F also improves the fusion of blurred images in layered rendering by radiance virtualization. Radiance virtualization transforms image intensity into scene radiance, and weighted layered rendering can generate better CoC results. In addition, we utilize the predicted defocus map as guidance for image fusion. Then we apply the Poisson gradient loss in our deep Poisson network to refine our initial fusion mask, which ensures the sharpness of in-focus parts. Exhaustive visualizations and ablation studies are presented to validate these modules and demonstrate their effects on the performance of D2F. We significantly enhance the quality of bokeh images. In the future, we can explore using dynamic filters for the selection of kernels and modify the defocus hallucination module to learn a more accurate single-channel defocus map.

Acknowledgement

This work was supported in part by the National Natural Science Foundation of China under Grant No. U1913602.

References

- [1] A. Ignatov, J. Patel, R. Timofte, Rendering natural camera bokeh effect with deep learning, in: Proceedings of the IEEE/CVF Conference on

- Computer Vision and Pattern Recognition Workshops, 2020, pp. 418–419.
- [2] X. Luo, J. Peng, K. Xian, Z. Wu, Z. Cao, Bokeh rendering from defocus estimation, in: European Conference on Computer Vision, Springer, 2020, pp. 245–261.
- [3] N. Wadhwa, R. Garg, D. E. Jacobs, B. E. Feldman, N. Kanazawa, R. Carroll, Y. Movshovitz-Attias, J. T. Barron, Y. Pritch, M. Levoy, Synthetic depth-of-field with a single-camera mobile phone, *ACM Transactions on Graphics (TOG)* 37 (4) (2018) 1–13.
- [4] B. Busam, M. Hog, S. McDonagh, G. Slabaugh, Sterefo: Efficient image refocusing with stereo vision, in: Proceedings of the IEEE International Conference on Computer Vision Workshops, 2019, pp. 0–0.
- [5] L. Wang, X. Shen, J. Zhang, O. Wang, Z. Lin, C.-Y. Hsieh, S. Kong, H. Lu, Deeplens: shallow depth of field from a single image, *arXiv preprint arXiv:1810.08100* (2018).
- [6] Y. Yang, H. Lin, Z. Yu, S. Paris, J. Yu, Virtual dslr: High quality dynamic depth-of-field synthesis on mobile platforms, *Electronic Imaging* 2016 (18) (2016) 1–9.
- [7] F. Banterle, A. Artusi, K. Debattista, A. Chalmers, *Advanced High Dynamic Range Imaging: Theory and Practice (2nd Edition)*, AK Peters (CRC Press), Natick, MA, USA, 2017.

- [8] Y. Cao, T. Zhao, K. Xian, C. Shen, Z. Cao, S. Xu, Monocular depth estimation with augmented ordinal depth relationships, *IEEE Transactions on Image Processing* (2018).
- [9] Y. Cao, Z. Wu, C. Shen, Estimating depth from monocular images as classification using deep fully convolutional residual networks, *IEEE Transactions on Circuits and Systems for Video Technology* 28 (11) (2017) 3174–3182.
- [10] C. Tang, L. Xinwang, X. Zheng, W. Li, J. Xiong, L. Wang, A. Zomaya, A. Longo, Defusionnet: Defocus blur detection via recurrently fusing and refining discriminative multi-scale deep features, *IEEE Transactions on Pattern Analysis and Machine Intelligence* (2020).
- [11] W. Zhao, X. Hou, Y. He, H. Lu, Defocus blur detection via boosting diversity of deep ensemble networks, *IEEE Transactions on Image Processing* 30 (2021) 5426–5438.
- [12] X. Zhang, R. Wang, X. Jiang, W. Wang, W. Gao, Spatially variant defocus blur map estimation and deblurring from a single image, *Journal of Visual Communication and Image Representation* 35 (2016) 257–264.
- [13] S. Bae, F. Durand, Defocus magnification, in: *Computer Graphics Forum*, Vol. 26, Wiley Online Library, 2007, pp. 571–579.
- [14] J. Lin, X. Ji, W. Xu, Q. Dai, Absolute depth estimation from a single defocused image, *IEEE Transactions on Image Processing* 22 (11) (2013) 4545–4550.

- [15] K. Xian, J. Zhang, O. Wang, L. Mai, Z. Lin, Z. Cao, Structure-guided ranking loss for single image depth prediction, in: The IEEE/CVF Conference on Computer Vision and Pattern Recognition (CVPR), 2020, pp. 611–620.
- [16] J. Shi, X. Tao, L. Xu, J. Jia, Break ames room illusion: depth from general single images, *ACM Transactions on Graphics (TOG)* 34 (6) (2015) 1–11.
- [17] H. Kumar, A. S. Yadav, S. Gupta, K. Venkatesh, Depth map estimation using defocus and motion cues, *IEEE Transactions on Circuits and Systems for Video Technology* 29 (5) (2018) 1365–1379.
- [18] Z. Zhang, C. Zhou, Y. Wang, W. Gao, Interactive stereoscopic video conversion, *IEEE transactions on circuits and systems for video technology* 23 (10) (2013) 1795–1808.
- [19] J. Shi, L. Xu, J. Jia, Just noticeable defocus blur detection and estimation, in: *Proceedings of the IEEE Conference on Computer Vision and Pattern Recognition*, 2015, pp. 657–665.
- [20] R. Yan, L. Shao, Blind image blur estimation via deep learning, *IEEE Transactions on Image Processing* 25 (4) (2016) 1910–1921.
- [21] C. Tang, J. Wu, Y. Hou, P. Wang, W. Li, A spectral and spatial approach of coarse-to-fine blurred image region detection, *IEEE Signal Processing Letters* 23 (11) (2016) 1652–1656.
- [22] S. Zhuo, T. Sim, Defocus map estimation from a single image, *Pattern Recognition* 44 (9) (2011) 1852–1858.

- [23] A. Levin, D. Lischinski, Y. Weiss, A closed-form solution to natural image matting, *IEEE transactions on pattern analysis and machine intelligence* 30 (2) (2007) 228–242.
- [24] G. Xu, Y. Quan, H. Ji, Estimating defocus blur via rank of local patches, in: *Proceedings of the IEEE International Conference on Computer Vision*, 2017, pp. 5371–5379.
- [25] H. Kumar, S. Gupta, K. Venkatesh, Simultaneous estimation of defocus and motion blurs from single image using equivalent gaussian representation, *IEEE Transactions on Circuits and Systems for Video Technology* 30 (10) (2019) 3571–3583.
- [26] J. Park, Y.-W. Tai, D. Cho, I. So Kweon, A unified approach of multi-scale deep and hand-crafted features for defocus estimation, in: *Proceedings of the IEEE Conference on Computer Vision and Pattern Recognition*, 2017, pp. 1736–1745.
- [27] C. Tang, C. Hou, Z. Song, Defocus map estimation from a single image via spectrum contrast, *Optics letters* 38 (10) (2013) 1706–1708.
- [28] A. Chakrabarti, T. Zickler, W. T. Freeman, Analyzing spatially-varying blur, in: *2010 IEEE Computer Society Conference on Computer Vision and Pattern Recognition*, IEEE, 2010, pp. 2512–2519.
- [29] R. Fontaine, A survey of enabling technologies in successful consumer digital imaging products, in: *Proceedings of the international image sensors workshop*, Hiroshima, Japan, Vol. 30, 2017.

- [30] C. Herrmann, R. S. Bowen, N. Wadhwa, R. Garg, Q. He, J. T. Barron, R. Zabih, Learning to autofocus, in: Proceedings of the IEEE/CVF Conference on Computer Vision and Pattern Recognition, 2020, pp. 2230–2239.
- [31] K. Xian, J. Peng, C. Zhang, H. Lu, Z. Cao, Ranking-based salient object detection and depth prediction for shallow depth-of-field, *sensors* 21 (5) (2021) 1815.
- [32] X. Zhang, K. Matzen, V. Nguyen, D. Yao, Y. Zhang, R. Ng, Synthetic defocus and look-ahead autofocus for casual videography, arXiv preprint arXiv:1905.06326 (2019).
- [33] P. P. Srinivasan, R. Garg, N. Wadhwa, R. Ng, J. T. Barron, Aperture supervision for monocular depth estimation, in: Proceedings of the IEEE Conference on Computer Vision and Pattern Recognition, 2018, pp. 6393–6401.
- [34] H. Tang, S. Cohen, B. Price, S. Schiller, K. N. Kutulakos, Depth from defocus in the wild, in: Proceedings of the IEEE Conference on Computer Vision and Pattern Recognition, 2017, pp. 2740–2748.
- [35] X. Lin, J. Suo, Q. Dai, Extracting depth and radiance from a defocused video pair, *IEEE Transactions on Circuits and Systems for Video Technology* 25 (4) (2014) 557–569.
- [36] M. Pharr, W. Jakob, G. Humphreys, Physically based rendering: From theory to implementation, Morgan Kaufmann, 2016.

- [37] P. Haeberli, K. Akeley, The accumulation buffer: hardware support for high-quality rendering, *ACM SIGGRAPH computer graphics* 24 (4) (1990) 309–318.
- [38] S. Lee, E. Eisemann, H.-P. Seidel, Real-time lens blur effects and focus control, *ACM Transactions on Graphics (TOG)* 29 (4) (2010) 1–7.
- [39] S. Dutta, Depth-aware blending of smoothed images for bokeh effect generation, *Journal of Visual Communication and Image Representation* 77 (2021) 103089.
- [40] J. Krivánek, J. Zara, K. Bouatouch, Fast depth of field rendering with surface splatting, in: *Proceedings Computer Graphics International 2003*, IEEE, 2003, pp. 196–201.
- [41] A. Robison, P. Shirley, Image space gathering, in: *Proceedings of the Conference on High Performance Graphics 2009*, 2009, pp. 91–98.
- [42] L. Xiao, A. Kaplanyan, A. Fix, M. Chapman, D. Lanman, Deepfocus: Learned image synthesis for computational display, in: *ACM SIGGRAPH 2018 Talks*, 2018, pp. 1–2.
- [43] I. De, B. Chanda, Multi-focus image fusion using a morphology-based focus measure in a quad-tree structure, *Information Fusion* 14 (2) (2013) 136–146.
- [44] M. S. Farid, A. Mahmood, S. A. Al-Maadeed, Multi-focus image fusion using content adaptive blurring, *Information fusion* 45 (2019) 96–112.

- [45] J. Ma, C. Chen, C. Li, J. Huang, Infrared and visible image fusion via gradient transfer and total variation minimization, *Information Fusion* 31 (2016) 100–109.
- [46] J. Ma, W. Yu, P. Liang, C. Li, J. Jiang, FusionGAN: A generative adversarial network for infrared and visible image fusion, *Information Fusion* 48 (2019) 11–26.
- [47] Z. Wang, Y. Ma, Medical image fusion using m-pcnn, *Information Fusion* 9 (2) (2008) 176–185.
- [48] R. Singh, A. Khare, Fusion of multimodal medical images using daubechies complex wavelet transform—a multiresolution approach, *Information fusion* 19 (2014) 49–60.
- [49] M. Uyttendaele, A. Eden, R. Szeliski, Eliminating ghosting and exposure artifacts in image mosaics, in: *Proceedings of the 2001 IEEE Computer Society Conference on Computer Vision and Pattern Recognition. CVPR 2001, Vol. 2*, IEEE, 2001, pp. II–II.
- [50] P. J. Burt, E. H. Adelson, The laplacian pyramid as a compact image code, in: *Readings in computer vision*, Elsevier, 1987, pp. 671–679.
- [51] P. Pérez, M. Gangnet, A. Blake, Poisson image editing, in: *ACM SIGGRAPH 2003 Papers*, 2003, pp. 313–318.
- [52] R. Szeliski, M. Uyttendaele, D. Steedly, Fast poisson blending using multi-splines, in: *2011 IEEE International Conference on Computational Photography (ICCP)*, IEEE, 2011, pp. 1–8.

- [53] J. Sun, H. Zhu, Z. Xu, C. Han, Poisson image fusion based on markov random field fusion model, *Information Fusion* 14 (3) (2013) 241–254.
- [54] H. Wu, S. Zheng, J. Zhang, K. Huang, Gp-gan: Towards realistic high-resolution image blending, in: *Proceedings of the 27th ACM international conference on multimedia*, 2019, pp. 2487–2495.
- [55] Z. Farbman, G. Hoffer, Y. Lipman, D. Cohen-Or, D. Lischinski, Coordinates for instant image cloning, *ACM Transactions on Graphics (TOG)* 28 (3) (2009) 1–9.
- [56] Z. Farbman, R. Fattal, D. Lischinski, Convolution pyramids., *ACM Trans. Graph.* 30 (6) (2011) 175.
- [57] Y. Liu, S. Liu, Z. Wang, A general framework for image fusion based on multi-scale transform and sparse representation, *Information fusion* 24 (2015) 147–164.
- [58] L. Zhang, T. Wen, J. Shi, Deep image blending, in: *Proceedings of the IEEE/CVF Winter Conference on Applications of Computer Vision*, 2020, pp. 231–240.
- [59] H. Lin, S. J. Kim, S. Süssstrunk, M. S. Brown, Revisiting radiometric calibration for color computer vision, in: *2011 International Conference on Computer Vision*, IEEE, 2011, pp. 129–136.
- [60] K. Xian, C. Shen, Z. Cao, H. Lu, Y. Xiao, R. Li, Z. Luo, Monocular relative depth perception with web stereo data supervision, in: *Proceedings of the IEEE Conference on Computer Vision and Pattern Recognition*, 2018, pp. 311–320.

- [61] J. Holm, I. Tastl, L. Hanlon, P. Hubel, Color processing for digital photography (2002).
- [62] X. Wang, K. Yu, S. Wu, J. Gu, Y. Liu, C. Dong, Y. Qiao, C. Change Loy, Esrgan: Enhanced super-resolution generative adversarial networks, in: Proceedings of the European Conference on Computer Vision (ECCV), 2018, pp. 0–0.
- [63] J. Johnson, A. Alahi, L. Fei-Fei, Perceptual losses for real-time style transfer and super-resolution, in: European conference on computer vision, Springer, 2016, pp. 694–711.
- [64] H. Zhao, O. Gallo, I. Frosio, J. Kautz, [Loss functions for image restoration with neural networks](#), IEEE Trans. Computational Imaging 3 (1) (2017) 47–57. doi:10.1109/TCI.2016.2644865.
URL <https://doi.org/10.1109/TCI.2016.2644865>
- [65] S. Xie, R. Girshick, P. Dollár, Z. Tu, K. He, Aggregated residual transformations for deep neural networks, in: Proceedings of the IEEE conference on computer vision and pattern recognition, 2017, pp. 1492–1500.
- [66] J. Deng, W. Dong, R. Socher, L.-J. Li, K. Li, L. Fei-Fei, Imagenet: A large-scale hierarchical image database, in: 2009 IEEE conference on computer vision and pattern recognition, Ieee, 2009, pp. 248–255.
- [67] A. Ignatov, R. Timofte, M. Qian, C. Qiao, J. Lin, Z. Guo, C. Li, C. Leng, J. Cheng, J. Peng, et al., Aim 2020 challenge on rendering realistic bokeh, in: European Conference on Computer Vision, Springer, 2020, pp. 213–228.

- [68] A. Ignatov, J. Patel, R. Timofte, B. Zheng, X. Ye, L. Huang, X. Tian, S. Dutta, K. Purohit, P. Kandula, et al., Aim 2019 challenge on bokeh effect synthesis: Methods and results, in: 2019 IEEE/CVF International Conference on Computer Vision Workshop (ICCVW), IEEE, 2019, pp. 3591–3598.
- [69] M. Qian, C. Qiao, J. Lin, Z. Guo, C. Li, C. Leng, J. Cheng, Bggan: Bokeh-glass generative adversarial network for rendering realistic bokeh, arXiv preprint arXiv:2011.02242 (2020).